Oliphant, C.J. et al. (2013). Characterization of silicon nitride thin films deposited by hot-wireCVD at low gas flow rates.
Applied Surface Science, 285P: 440 – 449.
http://dx.doi.org/10.1016/j.apsusc.2013.08.075

UNIVERSITY of the WESTERN CAPE

Characterization of silicon nitride thin films deposited by hot-wireCVD at low gas flow rates

Clive J. Oliphant, Christopher J. Arendse, Theophillus F.G. Muller and Dirk Knoesen

Abstract
We examined the chemical, structural, mechanical and optical properties of amorphous hydrogenated silicon nitride thin films deposited by hot-wire chemical vapour deposition using SiH_4, NH_3 and H_2 gases at total flow rates below 33 sccm. Time of flight secondary ion mass spectroscopy reveal that the film surfaces consist of predominantly Si with hydrogenated $Si_x N_y O_z$ species. Energy dispersive X-ray spectroscopy and X-ray photoelectron spectroscopy corroborate on the N/Si ratio. Electron energy loss spectroscopy discloses that the thickness of the nitrogen rich oxidized interface between the SiN_x films and the c-Si substrate decrease with an enhancing NH_3 flow rate. By varying the NH_3 flow rate, dense SiN_x films can be realized with hydrogen content between 16 and 9 at.%, a refractive index between 3.5 and 1.9 and optical band gap ranging from 2 to 4.5 eV. The SiN_x film stress is compressive for N/Si < 0.4 and tensile for higher N/Si > 0.55. Mechanisms relating the HWCVD conditions and the film structure and properties are proposed.

1. Introduction

Silicon nitride (SiN_x) is an important dielectric that enjoyed active research interest during the last few decades. SiN_x has been applied as surface and bulk passivation layers for solar cells [1], thin film transistors [2], antireflection coatings [3] and has shown promise as a light emitting material [4]. The wide application scope of SiN_x can be attributed to its refractive index, optical band gap, structural properties and molecular composition; all of which can be tuned by varying the deposition conditions [1,5,6].

Plasma enhanced chemical vapour deposition (PECVD) is the conventional synthesis technique for manufacturing SiN_x thin films. An alternative technique for the synthesis of SiN_x is hot-wire chemical vapour deposition (HWCVD). Compared to PECVD, SiN_x synthesized by HWCVD experience no ion bombardment and can be deposited at higher deposition rates [7] with reduced hydrogen content [8]. Despite the numerous studies on the synthesis of SiN_x from SiH_4 and NH_3 gas mixtures, reports on the effect of the addition of H_2 to the process gasses on the structure-property relationship

of SiN_x thin films has received less attention [9–11]. The benefits of adding H_2 to the usual NH_3/SiH_4 gas mixture include an enhanced incorporation of N into the thin film, reduced NH_3 flow rates down to 5 sccm and film conformity on the substrate [9–11]. In most cases, the filament temperature during the HWCVD of SiN_x films were >1700 °C [1–3,5,7–12], which can lead to filament metal impurities incorporated into the films [10,13].

In this study, we employ HWCVD to deposit transparent, low reflection, dense amorphous SiN_x thin films from a $SiH_4/NH_3/H_2$ gas mixture at a substrate temperature of 240 °C and a filament temperature of ~1600 °C. The total gas flow rate ranged from 30 to 33 sccm with that of NH_3 varied from 1 to 3 sccm, which is substantially lower than the usually deposition regime for SiN_x. In addition, we compare the N/Si compositional characterization of SiN_x thin films as probed by energy dispersive X-ray spectroscopy (EDS) and X-ray photoelectron spectroscopy (XPS). The internal structure and elemental distribution was investigated using high-resolution transmission electron microscopy (HR-TEM) and electron energy loss spectroscopy (EELS). We then propose a relationship between the HWCVD conditions, film structure, mechanical and optical properties.

2. Experimental procedure

2.1 Deposition conditions

SiN_x thin films were deposited simultaneously on Corning® 7059 and Si (1 0 0) substrates using a high vacuum MVSystems HWCVD system described elsewhere [14]. The deposition time, substrate temperature, deposition pressure, filament temperature, silane flow rate and hydrogen flow rate were fixed at 60 min, 240 °C, 150 μbar, 1600 °C, 2 sccm and 28 sccm, respectively. The NH_3 flow rate was varied from 1 to 3 sccm (in increments of 0.5 sccm).

2.2. Thin film characterization

The elemental composition of the SiN_x thin films were determined using XPS and EDS. XPS was performed in wide and narrow scan modes on a PHI® Quanta 2000 spectrometer using monochromatic $Al_{K\alpha}$ X-rays. EDS analysis was performed at 6 kV using a pure Si standard as the quantification optimization element in an OXFORD INCA EDS system in a Zeiss LEO 1525 field emission gun scanning electron microscope (FEGSEM). The bonding configuration of the SiN_x thin films were investigated using a PerkinElmer Spectrum 100 fast-Fourier transformed infrared (FTIR). The spectra were collected in transmission geometry from 400 to 4000 cm^{-1} with a spectral resolution of 1 cm^{-1}. The FTIR spectra were corrected for coherent and incoherent reflections [15,16]. The total hydrogen content in the film was determined using elastic recoil detection (ERD) analysis. The ERD analysis was conducted using a 3 MeV mono-energetic and collimated beam of $^4He^+$ ions

http://repository.uwc.ac.za

accelerated by the van de Graaff accelerator at iThemba Labs, in Cape Town, South Africa. The recoiled atoms were detected at an angle of 30° with respect to the incident ion beam. A Kapton reference material (coated with ~1 Å Pt) was used for energy and geometry calibration. The total H content was calculated from the ERD spectra using the SIMNRA simulation software.

Time of flight (ToF-SIMS) spectra of the SiN_x film surface were acquired using a TOF.SIMS5 system equipped with a Bi_1^{++} liquid metal ion source. Positive and negative ion spectra were accumulated with a pulsed beam current of 1 nA at 20 kV. Spectra were calibrated with hydrocarbons. The mass resolution was typically above 10,000. Raman spectra were recorded in backscattering geometry in the region 100–1300 cm^{-1} with a spectral resolution of 0.4 cm^{-1}, using a Jobin-Yvon HR800 micro-Raman spectrometer operated at an excitation wavelength of 514.5 nm. The power of the Raman laser was kept below 5 mW to avoid laser induced crystallization.

Cross-sections of the SiN_x films were prepared by a FEI Helios NanoLab 650 Dual Beam focussed-ion beam SEM (FIBSEM). Subsequently, high-resolution transmission electron microscopy (HRTEM) was performed on the cross-sections using a JEOL ARM 200F TEM. Electron energy loss spectroscopy (EELS) was performed in scanning transmission electron microscopy (STEM) mode at a step size of 4 nm × 4 nm to acquire Si, N and O elemental maps. The Gatan Quantum GIF energy filter was used to perform the EELS maps at a collection angle of 41.7 mrad. Electron diffraction was performed on a FEI Tecnai F20 FEGTEM at 200 kV. The film stress was estimated from curvature measurements determined on Corning (thermal expansion 4.6 μ/°C, Young's modulus 67.6 GPs and Poisson's ratio 0.28) substrates before and after deposition a using a Taylor stylus profilometer. The total film stress was then determined using Stoney's equation [17]. However, the total film tress is equal to sum of the intrinsic stress and the thermal stress. The thermal stress was determined from the constants for a-Si in [18] (thermal expansion coefficient 1 μ/°C, Young's modulus 130 GPa and Poison's ratio 0.28).

Optical transmission and reflection spectra were measured using a CARY 1E UV/VIS spectrophotometer in the range 200–900 nm with a spectral resolution of 1 nm. The refractive index, absorption coefficients and optical thickness were calculated by employing the Bruggeman effective medium approximation (BEMA) model [19].

http://repository.uwc.ac.za

3. Results and discussion

3.1 Film growth rate

Fig. 1 shows that the film growth rate increases as a function of NH_3 flow rate ($^{\circ}NH_3$). The maximum growth rates are competitive to that reported for PECVD [8,20] and also for some HWCVD studies [20]. However, the growth rates are still promising considering that we used a lower deposition pressure, filament temperature of 1600 °C and total gas flow rates lower by a factor of ~12 compared to that used in [7].

The HWCVD process of SiN_x is complex and can be divided into three stages, namely the dissociation of the NH_3, SiH_4 and H_2 gases at the filament, gas phase reactions and finally surface reactions at the substrate. During the gas dissociations at the heated Ta-filament; Si, N and H containing radicals are created, which can then proceed to the other two growth stages. However, filament degradation studies showed that the radicals diffuse within the Ta-filament; consequently resulting in the formation of Ta-nitrides and silicides. This depletion of growth species from the ambient can initially lead to inferior growth rates, especially in this study where the depositions were started with a pure Ta-filament surface. Afterwards, the silicide layer encapsulating the filament becomes thicker, which reduces the diffusion of radicals within the filament, i.e. more radicals are now available for the deposition leading to the higher growth rates at higher NH_3 flow rates.

Gas phase reactions are also a contributing factor to the film growth rate. The probability for a gas molecule to be dissociated by the heated filament surface is inversely proportional to the pressure and directly proportional to the square root of the filament temperature [21,22]. It is therefore possible that not all SiH_4 molecules are dissociated at our deposition conditions; given the deposition pressure of 150 μbar and low filament temperature of 1600 °C. However, the NH_3 partial pressure enhances with an increasing NH_3 gas flow rate. Coupled with the high H_2 concentration and the effectiveness of a heated filament to dissociate H_2 [23], there is expected to be a high concentration of atomic hydrogen during the deposition. Atomic hydrogen is unstable and can dissociate those SiH_4 molecules that were not dissociated by the heated filament [24]. Consequently an increase in growth rate occurs at higher NH_3 flow rates.

http://repository.uwc.ac.za

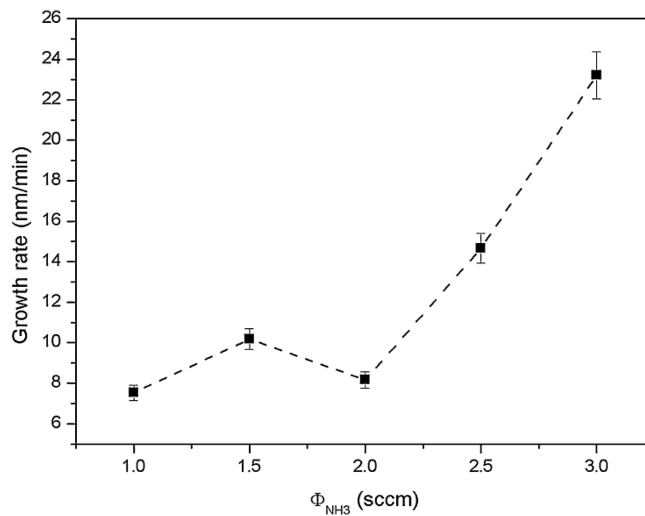

Fig. 1. Film growth rate at various NH_3 flow rates.

3.2. Compositional properties

Fig. 2 reveals that the hydrogen concentration, determined from ERD, decrease monotonically from ~16 at.% to ~9 at.% with an increase in $^{\circ}NH_3$. Fig. 3 shows deconvoluted XPS spectra of the Si 2p orbital for SiN_x thin films deposited at various $^{\circ}NH_3$. The spectra can be deconvoluted into three Gaussian peaks with centres at ~99.4 eV (Si Si), 103 eV (Si O) and 100.1 eV (Si N). The presence of the Si O peak indicates that the surface is oxidized. In addition, the simultaneous presence of Si Si and Si N reveal that the films are dual phase, i.e. the films are composed of a mixture of Si Si and Si N networks. Fig. 4a presents the relationship between the Si N area percentage (relative to Si O and Si Si) as a function of $^{\circ}NH_3$ flow rate. The concentration of the Si N bonds grows linearly with increasing NH_3 flow rate at the expense of the Si Si bonds, indicating an efficient use of the supply gases. This phenomenon has been observed before and was attributed to the gas phase dissociation of NH_3 by atomic hydrogen [9]. Fig. 4b shows an XPS depth profile for the sample deposited at $^{\circ}NH_3$ = 3sccm. The depth profile reveals that O and C are confined to the surface while homogenous atomic concentrations of N and Si constitute the bulk of the film.

The N/Si atomic ratio (x) is the most important factor that governs the electrical and optical properties of SiN_x. In general, the N/Si ratio is determined from Rutherford backscatter spectroscopy (RBS), heavy ion elastic recoil detection (ERD) [7], FTIR [9] or indirectly from the film refractive index [25]. However, the proportionality constants necessary for quantification from FTIR varies with film composition [26]; and the refractive index is influenced by the film density which, in turn, may also depend on the deposition technique [27]. Currently, scanning electron microscopes (SEM) are becoming increasingly accessible and coupled to a SEM in most cases is an energy dispersive X-ray spectroscopy (EDS) detector. EDS is used to identify and quantify elemental compositions of various elements with an atomic

http://repository.uwc.ac.za

number larger than 4 (Be). Despite its immense development for determining elemental compositions of bulk materials, EDS on thin films within the SEM have received less attention. This can be attributed to the beam penetration depth, issues relating to the homogeneity of the thin film (which will influence the quantification) and relatively high inaccuracies for low atomic number elements such as C. Nevertheless, with the advent of more sensitive detectors and enhanced detection levels at low acceleration voltages, EDS may be used as an alternative option to determine the elemental composition of SiN_x thin films.

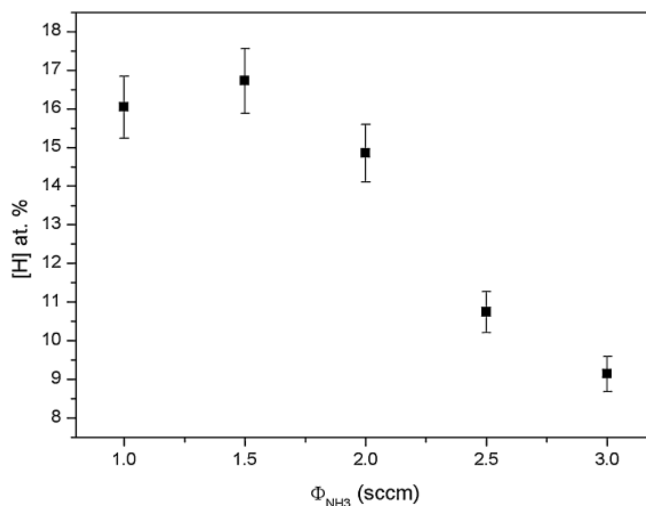

Fig. 2. Total hydrogen content as a function of Φ_{NH_3}.

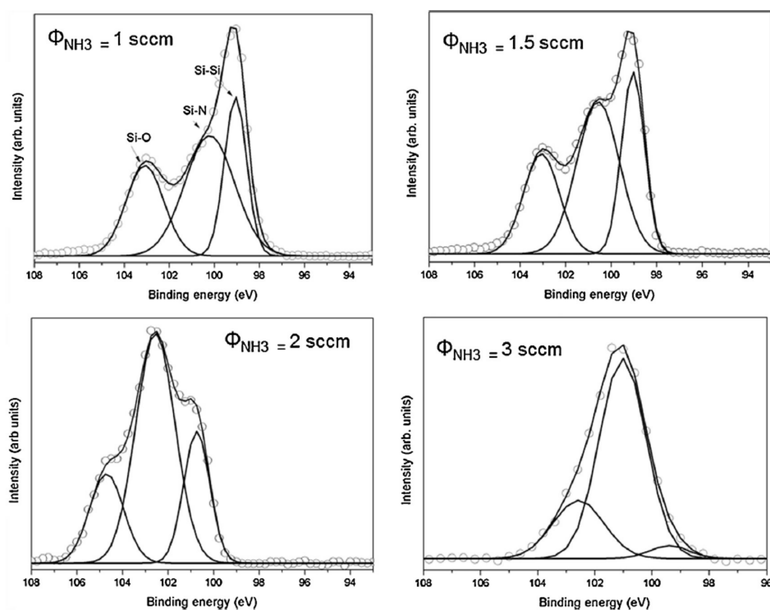

Fig. 3. XPS spectra of Si 2p level for SiN_x films deposited at various Φ_{NH_3}.

http://repository.uwc.ac.za

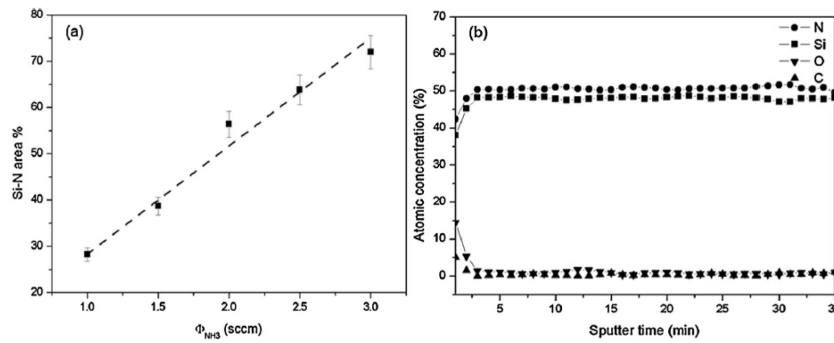

Fig. 4. (a) Si-N area percentage (with linear fit) at various NH_3 flow rates and (b) XPS elemental depth profile of the sample deposited at Φ_{NH_3} = 3sccm.

Table 1
Comparison between XPS and EDS. The values are within 5 at. % standard deviation. The total hydrogen content [H] was determined from ERD.

Φ_{NH_3} (sccm)	$[N]_{XPS}$(at.%)	$[N]_{EDS}$(at.%)	$[Si]_{XPS}$(at.%)	$[Si]_{EDS}$ (at.%)	[H] (at.%)	x_{XPS}	x_{EDS}
1	15.66	18.65	68.30	65.31	16.04	0.23	0.29
1.5	20.90	22.33	62.38	60.95	16.72	0.34	0.37
2	30.72	31.02	54.43	54.13	14.85	0.56	0.57
2.5	42.31	45.45	46.95	43.81	10.74	0.90	1.03
3	47.01	49.27	43.85	41.59	9.14	1.07	1.18

Presented in Table 1 is a comparison between the N and Si atomic percentages determined from XPS and EDS; showing the good correlation between these two independent techniques. The values are adjusted to include the H-content determined from ERD.

FTIR is the preferred technique used to determine and quantify the bonding configurations of SiN_X thin films. Fig. 5 shows a typical FTIR spectrum of a SiN_X sample revealing the presence of four peaks: the Si N (stretching) mode near 850 cm^{-1}, N H bending mode at 1200 cm^{-1}, the Si H stretching mode near 2190 cm^{-1} and the N H stretching mode at 3330 cm^{-1} [26]. The amounts of the Si N, N H and Si H bonds can be obtained from the relevant infrared absorption bands by:

$$[X-Y] = A_{X-Y} \int \frac{\alpha(\omega)}{\omega} \quad (1)$$

where ‸(ω) is the absorption coefficient at wavenumber ω and A_{X-Y} is the proportionality coefficient.

http://repository.uwc.ac.za

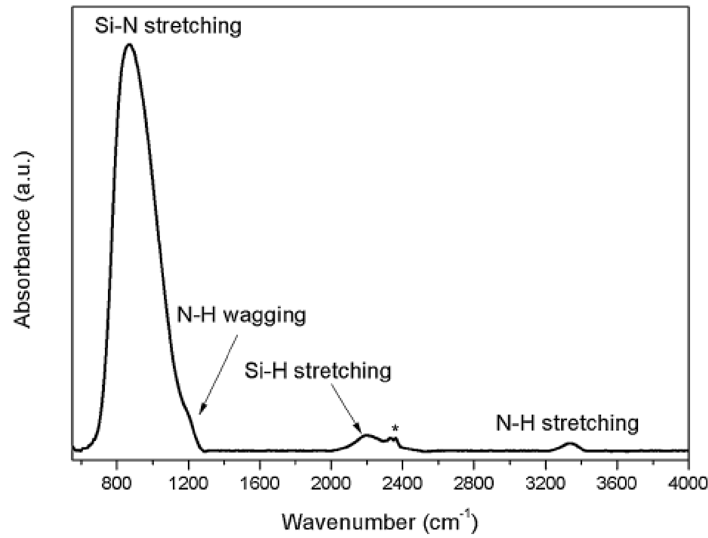

Fig. 5. Typical FTIR spectrum of the sample deposited at 3 sccm NH_3. The peaks indicated by * correspond to fluctuations in the CO_2 concentrations within the spectrometer which were consequently not properly removed by the background.

The proportionality coefficients proposed by Lanford and Rand [28] for the N H and Si H bond concentrations were used. For the [Si N] the average value of 1.4×10^{19} cm^{-2} was chosen as proposed by Verlaan et al. [5]. Then, assuming the absence of H H and N N bonds in the thin films [5,25,29], the atom concentrations of H, N and Si can be determined by the following set of equations [30]:

$$[H] = [Si{-}H] + [N{-}H] \quad (2)$$

$$[N] = \frac{[Si{-}N] + [N{-}H]}{3} \quad (3)$$

$$[Si] = \frac{[Si{-}N] + [Si{-}H]}{4} + \frac{[Si{-}Si]}{2} \quad (4)$$

The [Si—Si] bond density can be derived from Eq. (4) and $[Si] = [N]/x$ as:

$$[Si - Si] = 2\frac{[N]}{x} - \frac{[Si - N] + [N - H]}{2} \quad (5)$$

Fig. 6 presents the FTIR atomic concentrations of [H], [N], [Si] and [Si Si]. A relatively higher concentration of [Si Si], [Si] and [H] exist at N/Si ≤ 0.30, which then decrease with an increasing N/Si ratio. Initially, the [N] atomic concentration is in inferior amounts, which then gradually increase with an increasing N/Si ratio. The values of the atomic concentrations are relatively inferior compared to that reported for SiN_x films deposited from SiH_4 and NH_3 mixtures [5,30] (the studies used the same proportionality factors), which indicates an increase in defects as the NH_3 flow rate increases. The peak position of

http://repository.uwc.ac.za

the Si H bond is influenced by the composition of the SiN_x films [7] and more specifically, the different types of back bonding of the hydrogenated Si atom [25]. Fig. 6b reveals that the peak position of S H scales linearly with N/Si. The absence of NH_3 from the gas mixture in this study will result in the deposition of microcrystalline silicon instead of amorphous silicon, due to the high H_2 dilution used in this study, which favours the crystallization of silicon [31]. The Si H peak position at 2092 cm^{-1} (N/Si = 0) falls within the range expected for microcrystalline silicon [32] and is close to 2220 cm^{-1} for N/Si ~1.33 corresponding to a-Si_3N_4 [1].

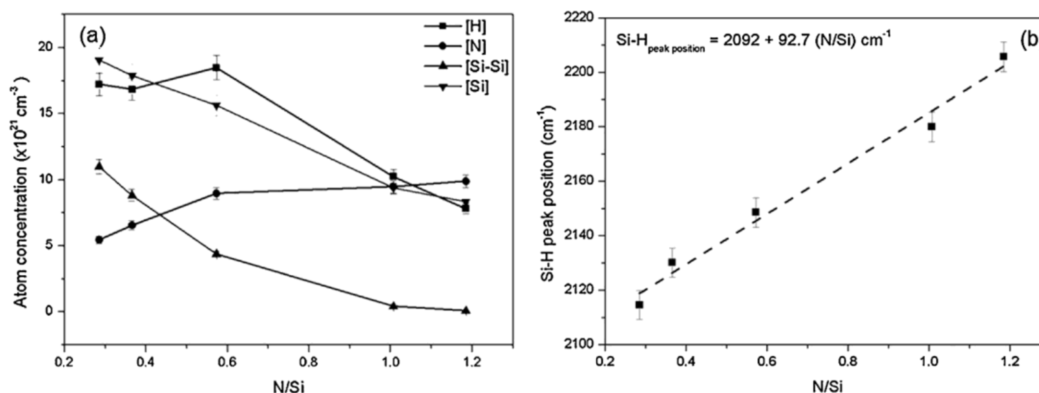

Fig. 6. (a) FTIR atomic concentrations and (b) variation of the Si H peak position as a function of N/Si.

ToF-SIMS is a sensitive analytical technique that is useful to interrogate the chemical structure and composition of surfaces. However, the application of ToF-SIMS for characterizing SiN_x thin films synthesized by HWCVD is quite rare [33]. In this study, ToF-SIMS was used to determine if metal impurities from the filament were incorporated into the film and whether the surface composition followed trends seen in FTIR, ERD, XPS and EDS. Fig. 7 presents positive ion ToF-SIMS spectra of SiN_x films with various N/Si ratios. The most intense peak is the Si^+ peak at 27.99 m/z, against which the spectra was normalized. The most dominating Si H signal is the SiH^+ peak centred at 28.98 m/z, with fewer contributions from SiH_2 and SiH_3. The most intense Si N based signal is the $SiNH_2^+$ peak at 44 m/z. Other noteworthy peaks are related to various hydrocarbons and oxides. The presence of C and O signals indicate contaminated oxidized surfaces, corroborating the XPS analysis. No heavy metal based (Ta) peaks were observed, indicating no contamination from the filament or at most below the ToF-SIMS detection limit. Negative ion spectra (not shown here) contained similar peaks, although H was the most intense peak.

Fig. 7b and c shows that the relative intensity of the SiH and the H signal decreases with an enhancing N/Si ratio, correlating to the trends shown by the FTIR and ERD analysis. The trends in the relative intensities of the $SiNH_2^+$ and oxides (not shown here) was irregular with an enhancing NH_3 flow rate.

http://repository.uwc.ac.za

An increase in the NH_3 flow rate results in an enhancement in the incorporation of N into the film. The Si N and Si H bonds are more energetically favoured than Si Si bonds [34]. Consequently, the Si Si bonding decreases at the expense of the Si N bonds as the N content within the film enhances.

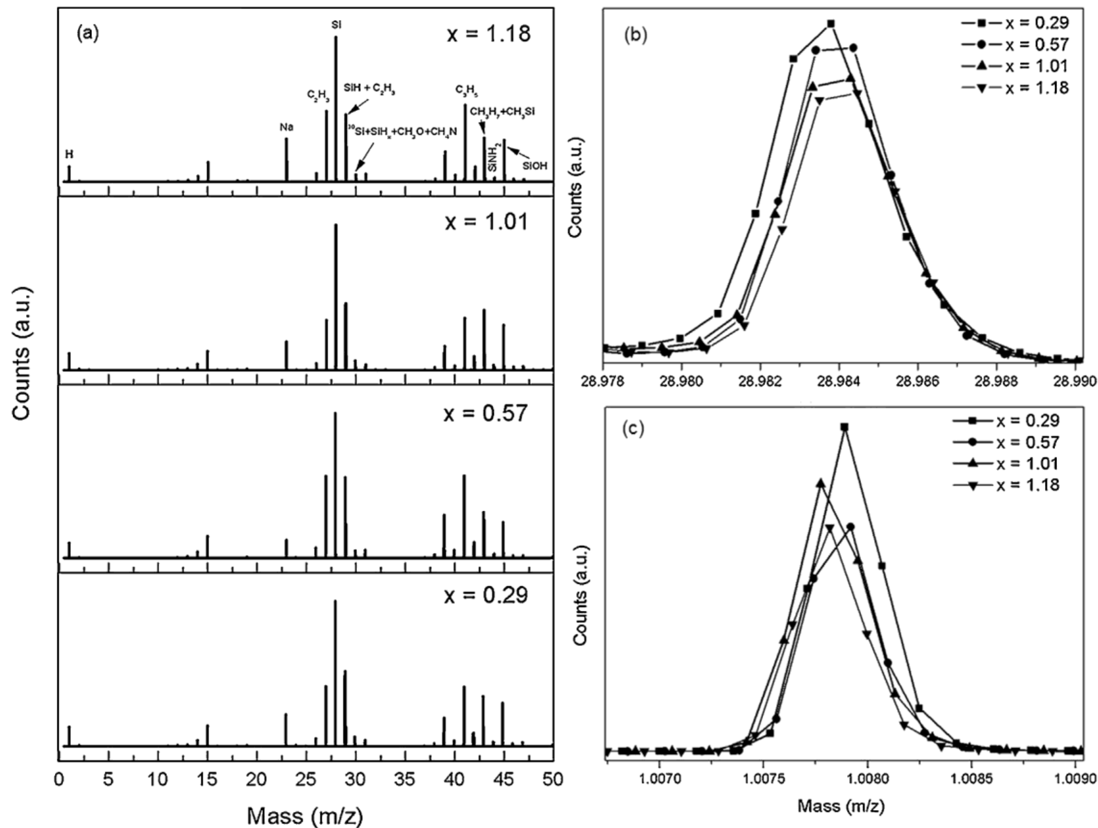

Fig. 7. (a) Normalized ToF-SIMS spectra (positive mode) of the SiN_X surface, (b) SiH and (c) H signals at various N/Si ratios.

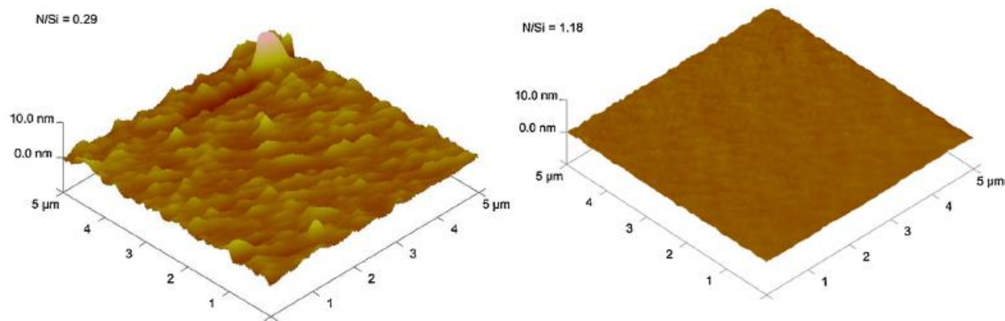

Fig. 8. 3D AFM micrographs of the SiN_x films at different N/Si ratios.

However, the number of Si H bonds and H concentration decreased at higher NH_3 flow rates. Verlaan et al. [35] observed similar trends and attributed the decreasing Si H and H-concentration to cross-linking reactions within the film, i.e. the formation of Si N and H_2 (released as gas [36]) bonds via the reactions of N H with Si H bonds.

http://repository.uwc.ac.za

3.3. Film microstructure

The surface roughness of SiN_x thin films is an important parameter to be considered in thin film transistors and anti-reflective coatings for solar cells. Fig. 8 shows representative 3D AFM images of SiN_x thin films with varying N-content. The root-mean-square (RMS) roughness values shown in Fig. 9 reveals that the surface roughness decreases to a minimum value of ~0.15 nm, substantially lower than that reported for HWCVD of SiN_x using a SiH_4 and NH_3 mixture [37].

Atomic hydrogen is released as a by-product during the decomposition of NH_3 [38]. Therefore, an increased NH_3 flow rate leads to an increasing atomic hydrogen concentration. The subsequent high concentration of atomic hydrogen can then result in an improved H-terminated surface, thereby promoting the diffusion of radicals on the surface, which can lead to smoother surfaces [39]. The internal structure of the SiN_x thin films were investigated by TEM and EELS. Fig. 10 shows TEM micrographs of the SiN_x films at $x = 0.29$ and $x = 1.18$. The films are amorphous as indicated by electron diffraction patterns (insets in Fig. 10) and are dense, which is suitable for device applications. The film thickness increased with an increasing NH_3 flow rate, confirming the UV–vis and profilometer measurements. Fig. 11 presents EELS elemental maps of Si, N and O. Despite the thickness of the cross-sections being less than at most half the inelastic electron mean free path at 200 kV, the EELS maps are qualitative in that it was not possible in the current TEM set-up to monitor the intensity and position of the zero-loss peak while acquiring the elemental maps. Nevertheless, valuable qualitative information about the Si, N and O profiles within the SiN_x can be extracted from EELS.

The O-signal is intense at the SiN_x/c-Si substrate interface and at the SiN_x surface. The presence of an oxide between the SiN_x and the substrate indicates that the HF dip was not effective in removing the native oxide from the c-Si substrate. Confirming the XPS and ToF-SIMS findings are surface oxide layers on the SiN_x films. However, oxidation subsequent to the FIB sample preparation also occurs and contributes to the O-signal throughout the SiN_x/c-Si cross-sections as revealed by the similar O-signal intensities at the C-coating, SiN_x film bulk and the c-Si substrate.

The intensity of the EELS N-signal is homogenous throughout the SiN_x films and enhances relative to the Si-signal with an increasing N/Si ratio; indicating an enriching N-content within the films, which supports the XPS, EDS and FTIR analysis. Furthermore, there are regions within the N- and Si-signals that have different brightness; indicating nanosized regions with Si- and/or N-rich areas. Interestingly, a nitrogen rich silicon oxide interface resides between the SiN_x and c-Si substrate. The thickness of the silicon oxynitride layer decreased from ~30 nm to 10 nm as the NH_3 flow rate increases from 1 to 3 sccm.

http://repository.uwc.ac.za

XRD analysis (not shown here) confirmed the absence of crystallinity from the deposited SiN_x thin films. Raman spectroscopy is a powerful tool for probing the structure of Si based thin films. Fig. 12 presents the Raman spectra for samples with different N/Si ratios. The dual phase nature of the films is clear through the simultaneous presence of a-Si transverse optic (TO) peak at ~480 cm^{-1} with the 2nd order TO peak at ~930 cm^{-1} and SiN_x peaks at ~800 cm^{-1} [40,41]. Samples with a higher N/Si ratio displayed additional SiN_x peaks at 700 cm^{-1} and 1150 cm^{-1} [41]. The absence of the c-Si TO peak at ~515 cm^{-1} indicates that there is no detectable crystallinity [42], confirming the TEM and XRD analysis. The Raman spectra were deconvoluted into Gaussian peaks corresponding to a-Si and SiN_x as shown in Fig. 13. Fig. 14 shows the integrated intensity ratio of the SiN_x and a-Si TO peaks ($I_{SiNx}/I_{a\text{-}Si}$), revealing that it increases with an increasing N/Si ratio, which is indicative of an increasing fraction of SiN_x, corroborating the XPS and FTIR results. The full width at half maximum (FWHM) of the a-Si TO peak increases with an enhancing N/Si ratio, whereas the FWHM of the SiN_x peak increases until N/Si ~0.6 and then decreases at higher N values. This can be interpreted as the ordering within the a-Si network is relatively enhanced within Si-rich SiN_x films.

Fig. 15 presents the integrated intensity ratio $17 = I_{2TO}/I_{TO}$ of a-Si; disclosing that it increases monotonically with an increasing N/Si ratio.

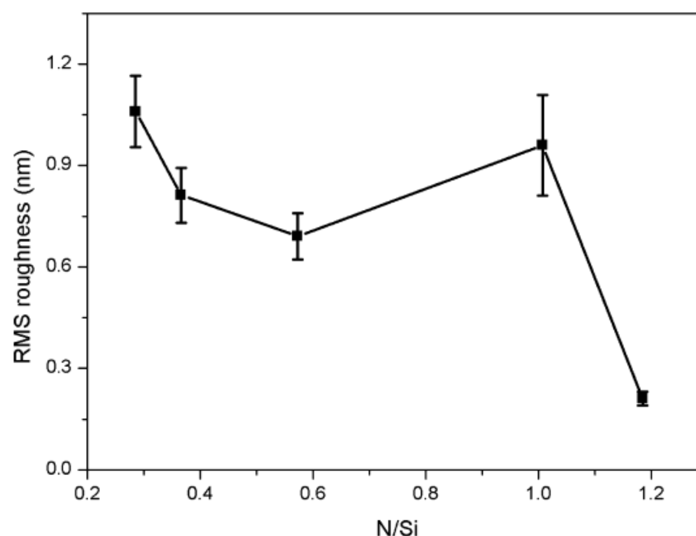

Fig. 9. RMS roughness values at various N/Si ratios.

http://repository.uwc.ac.za

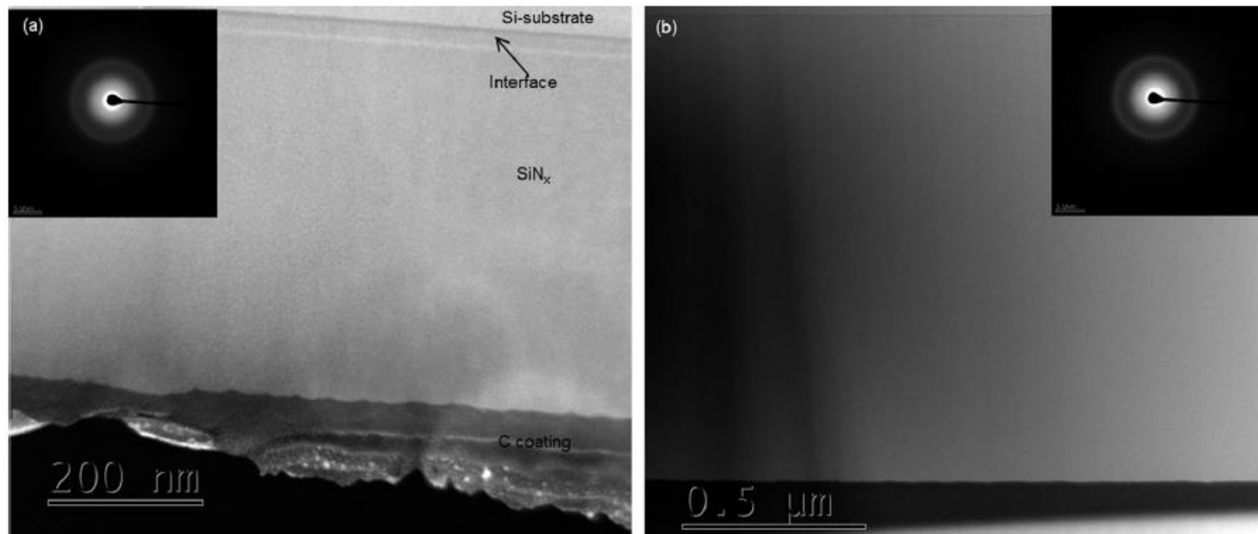

Fig. 10. TEM micrographs of the SiN_x thin films at (a) N/Si = 0.29 and (b) 1.18. The insets show diffraction patterns in each case.

Initially, 17 = 0.22, is below the value of 0.25 for a-Si and above that of bulk c-Si of 0.10 [43]. Subsequently, 17 transcends the value for a-Si reaching values of ~0.62 for samples with high N-content. Mercaldo et al. [40] observed a 17 ~ 1 and attributed it to size-dependent enhanced electron-phonon coupling in amorphous or crystalline nanostructures within a SiN_x thin film.

However, in this study it was not possible to directly analyze regions smaller than 4 nm using EELS. Additionally, the samples experienced damage after prolonged exposure to the 200 kV electron beam. Nevertheless, the nanoscale regions of brightness in the EELS Si-maps and the simultaneous presence of Si Si and Si N bonds suggest that nanosized Si-rich regions may be present within the SiN_x thin films.

Moreover, the disorder increases within the Si Si regions as more N is incorporated. The cross-section of the a-Si TO Raman peak is largely determined by the deformation potential involving short-range interaction between the Si Si lattice displacement and electrons [44]. Adapting this to amorphous materials, the enhancing defects (corresponding to an increasing tensile stress) induces an enlarging displacement which reduces the TO scattering cross-section and eventually higher I_{2TO}/I_{TO} ratios at higher N/Si values.

Regardless of the high hydrogen dilution used in this study, no crystallization occurred as revealed by XRD, Raman spectroscopy and electron diffraction in the TEM analysis. This can be explained by the increased incorporation of nitrogen and the decrease of the H-content as the N/Si ratio increases, which create defects within the SiN_x thin films. Coupled with the low substrate temperature of 240 °C, this impedes crystallization. The increasing number of defects results in the observed decreasing FTIR bonding densities and the observed disordering within the Si Si

http://repository.uwc.ac.za

regions as shown by Raman spectroscopy. Wanka and Schubert [45] reported on the effective etching of a native oxide film on silicon by atomic hydrogen generated by a heated filament. In line with the findings by Wanka and Schubert [45] the reduction in the oxide thickness between the SiN_x/c-Si interface as the NH_3 flow rate increases is attributed to an enhancing etching by atomic hydrogen.

The presence of a nitrogen-rich interface between the SiN_x and the underlying c-Si substrate is attributed to the diffusion of N within the oxide layer.

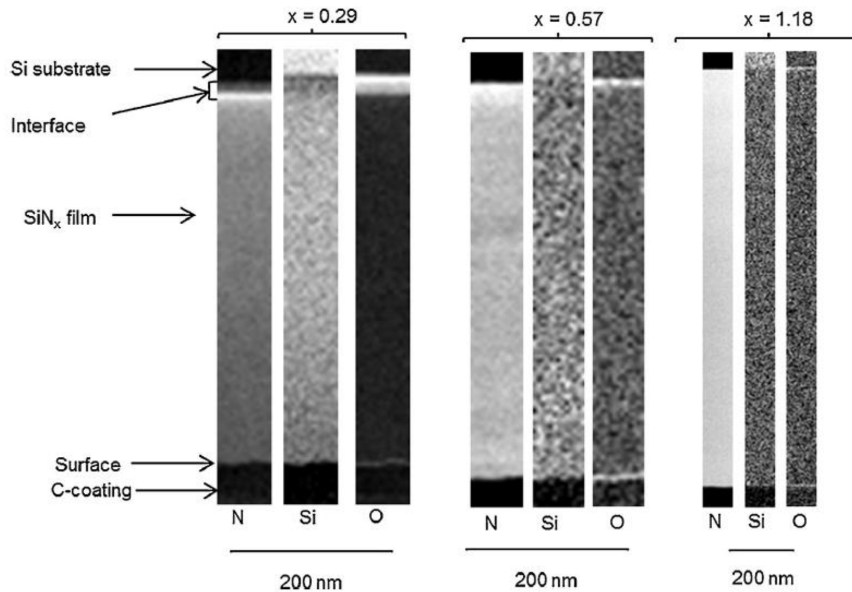

Fig. 11. Normalized EELS elemental N, Si and O maps of the SiN_x thin films with different N/Si ratios.

http://repository.uwc.ac.za

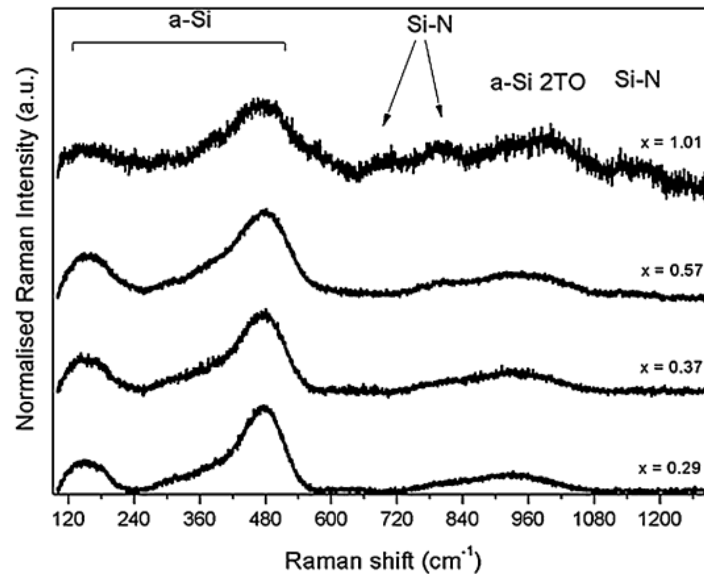

Fig. 12. Raman spectra of the SiN_x samples with varying N/Si ratios.

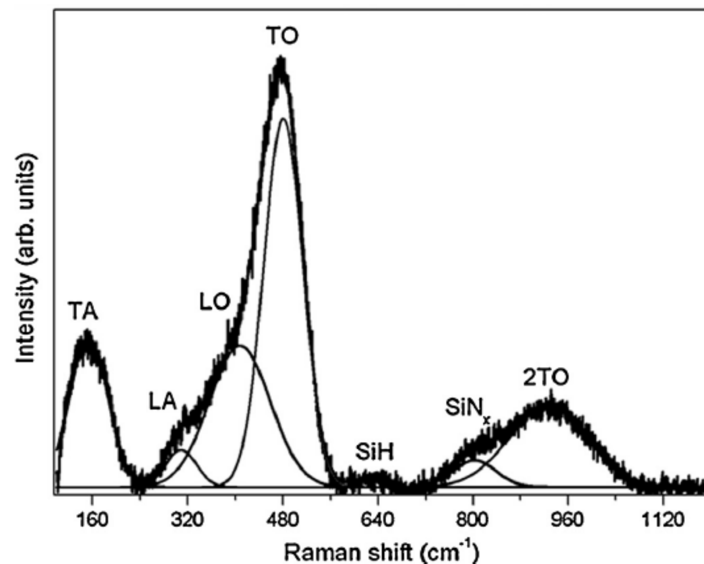

Fig. 13. Deconvoluted Raman spectrum of a SiN_x sample. The a-Si peaks labelled TO, 2TO LO, LA and TA are present with peaks for SiN_x and SiH.

The N atoms then passivate the dangling bonds within the oxide by forming energetically favoured Si N bonds, resulting in a nitrogen-rich interface. Fukuda et al. [46] reported similar findings in their thermally oxynitridation studies of a Si (1 0 0) wafer. The reduction of the N-rich interface-thickness with an increasing NH_3 flow rate is due to the reduction in the native oxide thickness owing to the enhancing etching of atomic hydrogen. Coupled to a higher H density, the dangling bonds within the interface are passivated by hydrogen reducing the areas where N can bond, subsequently resulting in a decreasing N-rich interface. The presence of defects within the SiN_x thin films further manifest in the form of film stress. Fig. 16 shows the film stress as a function of N/Si; revealing that the film is under compresive stress for $x < 0.4$ and then under tensile stress

http://repository.uwc.ac.za

for $x > 0.55$. Hasegawa et al. [47] also observed a change in stress from compression to tensile at N/Si ~ 0.5 and attributed it to the rearangment in the Si N network.

Specifically, the distance between Si and N becomes shortened within the distorted bonding arrangment leading to a contraction of the films as the N content increases; ultimately leading to tensile stress [47]. Additionally, the inreasing deposition rate as the NH_3 flow rate enhances in this study results in a higher supply rate of radicals compared to the rate of Si, H and N incorporation wihin the SiN_x thin films consequently, resulting in the deposition of a disordered, tensile network at N/Si > 0.55.

3.4. Optical properties and film stress

The understanding of the optical properties of SiN_x films is vital considering that they can be applied as anti-reflective coatings on solar cells. Fig. 17 presents the dispersion in the absorption coefficient and refractive index at vaiours photon energies. The refractive index and absorption coefficient decrease with an enhancing N content within the films.

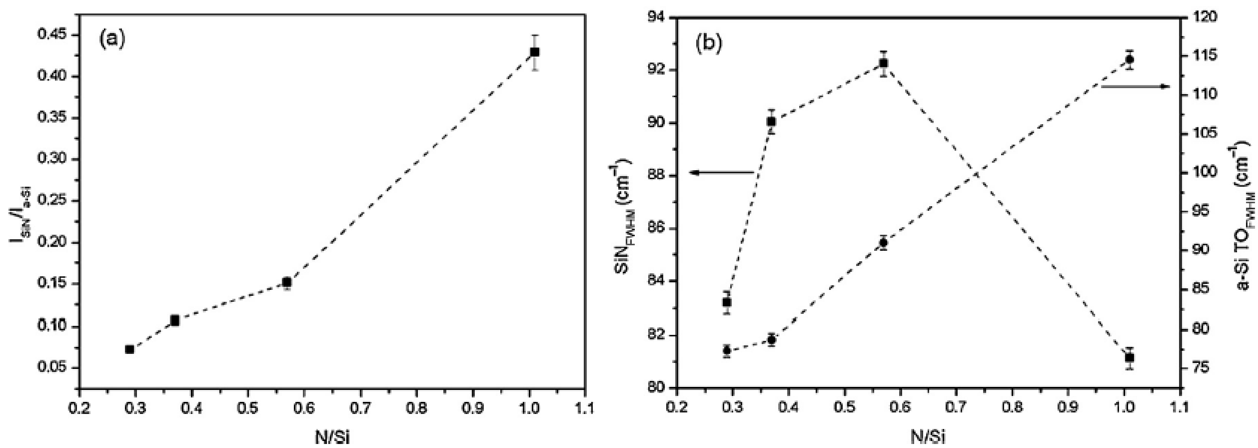

Fig. 14. (a) Intensity ratio of the a-Si TO peak to the SiN_x peak and (b) variation of the FWHM of the SiN_x and a-Si TO peaks at different N/Si ratios.

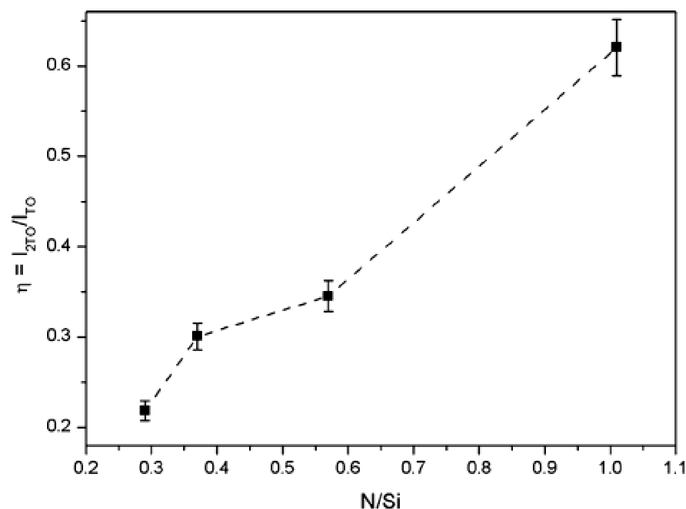

Fig. 15. Intensity ratio of second- to first-order of a-Si at various N/Si ratios.

http://repository.uwc.ac.za

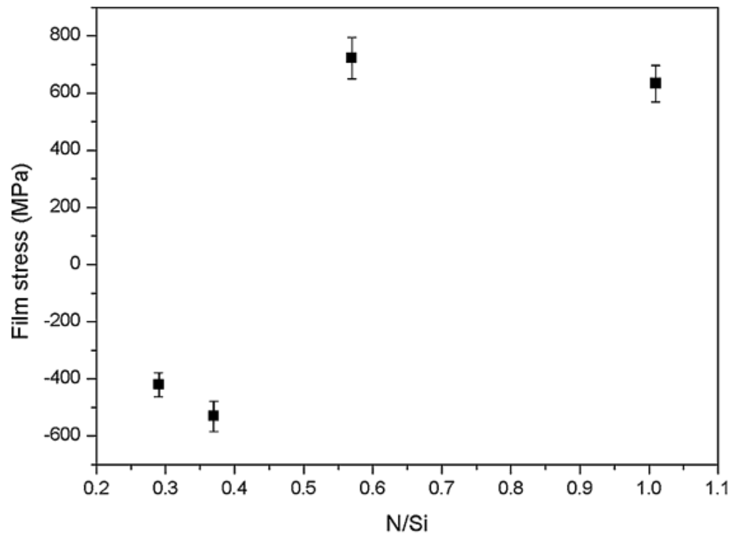

Fig. 16. Intrinsic film stress at various N/Si ratios.

This trend is consistent with the enhancing SiN phase as observed by XPS. Fig. 18 shows the refractive index (n) at 632 nm and the extintion coeffifcient (k) at 400 nm of the SiN_x thin films as a function of N/Si. The refractive index decrease linearly with an increasing N/Si ratio according to:

$$n_{632nm} = 3.92 - 1.81\left(\frac{N}{Si}\right) \quad (6)$$

The extrapolated n_{630nm} value of 3.92 ± 0.21 at N/Si = 0 is close to the value reported for microcrystalline silicon of 3.75 [48]. The expected value of n_{632nm} = 1.51 ± 0.24 at N/Si ~ 1.33 is lower than the value of 1.90 for a-Si_3N_4 and is attributed to the presence of tensile stress observed for SiN_x ($x > 0.57$) thin films in this study.

The enhancing incorporation of N within the film results in the increasing number of the energetically favoured Si N bonds [34] and a reduction in the [Si Si] bonds. Fig. 18b shows that a noticeable reduction of k_{400nm} occurs with an increase in the N/Si ratio, which idicate less absorption within the visible wavelenght regions. Fig. 19 shows the Tauc band gap of the SiN_x layers disclosing that the band gap widens linearly with an increase in N/Si according to:

$$E_{Tauc} = 1.31 + 2.49\left(\frac{N}{Si}\right) \quad (7)$$

http://repository.uwc.ac.za

The relation expressed in Eq. (7) differs from that reported for the deposition of SiN_x from SiH_4 and NH_3 gas mixtures [49].

Nevertheless, the E_{Tauc} values reduces to 1.31 eV at N/Si = 0; corresponding well with the reported value for microcrystalline silicon [32] and to 4.63 eV, which is approaching 5 eV for Si_3N_4 [50].

The Tauc optical band gap increased linearly with an enhancing N/Si ratio. Conversely, the refractive index decreased linearly with an increasing N/Si ratio. The behaviour of the optical properties corresponds well to the increasing N and Si N concentration, regardless of the presence of $Si_xN_yO_z$ interfaces. These interfaces are relatively low in concentration compared to the SiN_x bulk and therefore changes within the chemical composition especially N incorporation into the SiN thin films dominate the optical properties.

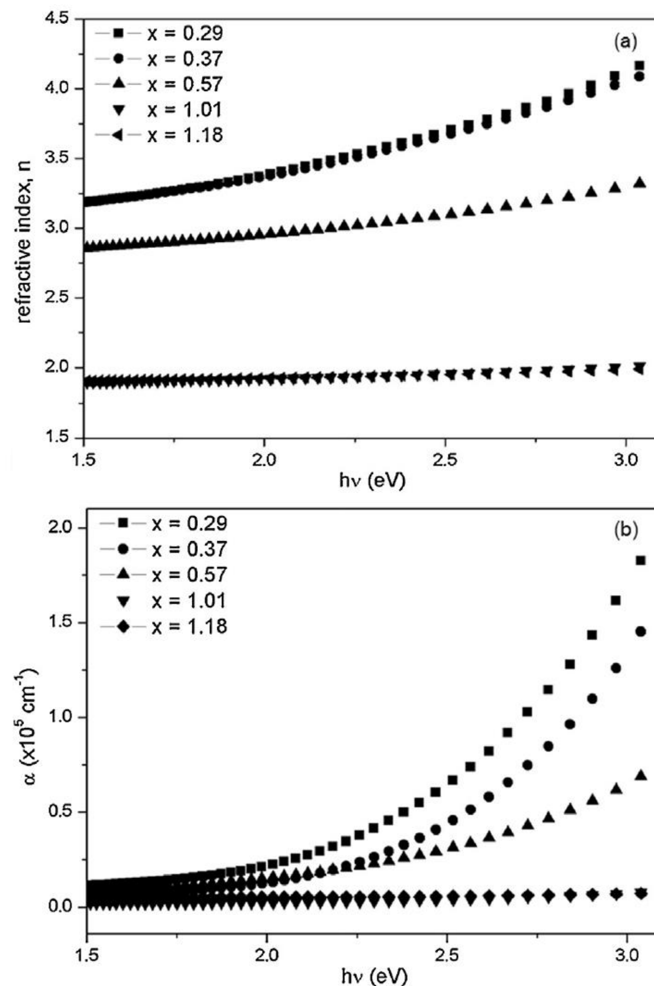

Fig. 17. Dispersion in the (a) refractive index and (b) absorption coefficient of SiN_x thin films with various N/Si ratios.

http://repository.uwc.ac.za

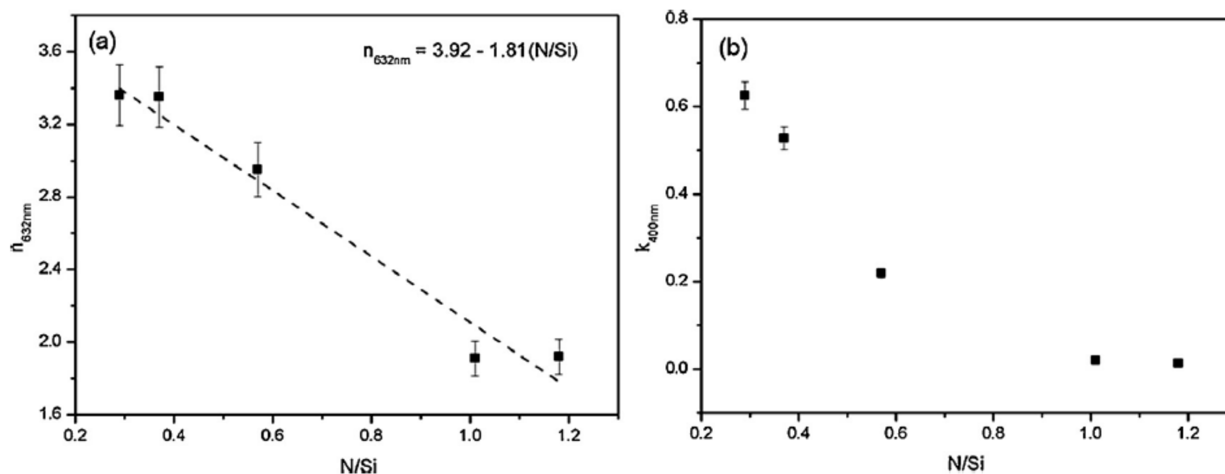

Fig. 18. (a) Refractive index at 632 nm and (b) extinction coefficient at 400 nm as a function of N/Si.

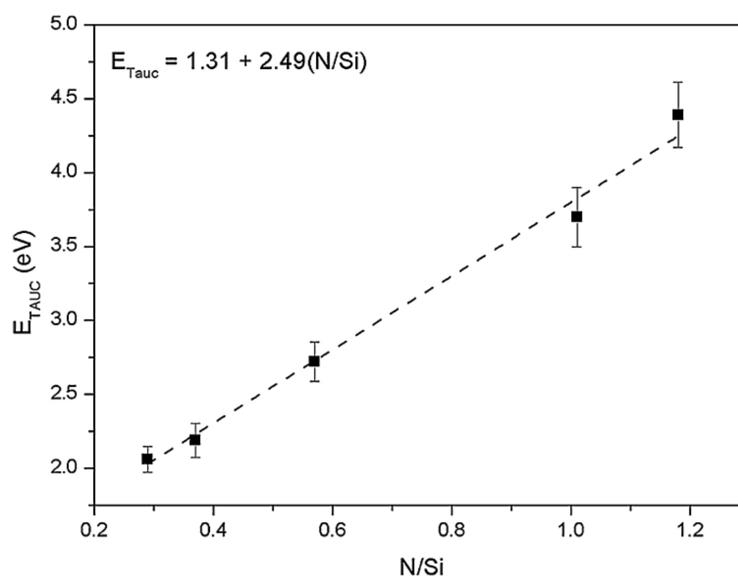

Fig. 19. Tauc optical band gap as a function of N/Si ratio.

4. Conclusion

The chemical composition, bonding densities, stress and optical properties of hydrogenated SiN_X thin films as a function of NH_3 flow rate synthesized by HWCVD have been studied. Independent XPS and EDS analysis corroborate each other on the determination of the N/Si ratio. Nitrogen from the NH_3 gas was effectively incorporated into the film, while the hydrogen content decreased with an increasing N/Si ratio. The band gap of the SiN_X thin films increased with an enhancing N/Si ratio. Conversely, the refractive index decreased with an increasing N/Si ratio. Compressive film stress occurred in Si-rich SiN_X thin films, which decreases and then changed to tensile stress as the N content increase. Filament degradation and gas phase reactions determined the SiN_X growth rate. The increasing incorporation of N within the SiN_X thin films created defects, regardless of the improved etching by atomic hydrogen as the NH_3 flow rate is increased. Nevertheless, highly transparent, H-containing and low reflection SiN_X layers

http://repository.uwc.ac.za

with smooth surfaces were deposited, which is promising for applications as anti-reflective coatings and passivation layers on solar cells.

Acknowledgements

The authors acknowledge the financial support of the National Research Foundation (NRF), the Department of Science and Technology (DST) and the National Metrology Institute of South Africa (Project no, TP021). The authors are thankful to Mr. P. Greeff, National Metrology Institute of South Africa, for helping with the film stress measurements. Dr. D. Motaung, National Centre for Nanostructured Materials, is acknowledged for assistance with the XRD, FTIR and Raman measurements.

http://repository.uwc.ac.za

References

[1] V. Verlaan, C.H.M. van der Werf, Z.S. Houweling, I.G. Romijn, A.W. Weeber, H.F.W. Dekkers, H.D. Goldbach, R.E.I. Schropp, Prog. Photovoltaics Res. Appl. 15 (2007) 563.

[2] B. Stannowski, J.K. Rath, R.E.I. Schropp, Thin Solid Films 395 (2001) 339.

[3] R.E.I. Schropp, C.H.M. van der Werf, V. Verlaan, J.K. Rath, H. Li, Thin Solid Films 517 (2009) 3039.

[4] N. Park, C. Choi, T. Seong, S. Park, Phys. Rev. Lett. 86 (2001) 1355.

[5] V. Verlaan, A.D. Verkerk, W.M. Arnoldbik, C.H.M. van der Werf, R. Bakker, Z.S. Houweling, I.G. Romijn, D.M. Borsa, A.W. Weeber, S.L. Luxembourg, M. Zeman, H.F.W. Dekkers, R.E.I. Schropp, Thin Solid Films 517 (2009) 3499.

[6] F. Giorgis, F. Giuliani, C.F. Pirri, E. Tresso, C. Summonte, R. Rizzoli, R. Galloni, A. Desalvo, P. Rava, Philos. Mag. B 77 (1998) 925.

[7] V. Verlaan, Z.S. Houweling, C.H.M. van der Werf, I.G. Romijn, A.W. Weeber, H.D. Goldbach, R.E.I. Schropp, Thin Solid Films 516 (2008) 533.

[8] A. Masuda, H. Umemoto, H. Matsumara, Thin Solid Films 501 (2006) 149.

[9] A.H. Mahan, A.C. Dillon, L.M. Gedvilas, D.L. Williamson, J.D. Perkins, J. Appl. Phys. 94 (2003) 2360.

[10] F. Liu, S. Ward, L. Gedvilas, B. Keyes, B. To, Q. Wang, E. Sanchez, S. Wang, J. Appl. Phys. 96 (2004) 2973.

[11] Q. Wang, S. Ward, L. Gedvilas, B. Keyes, E. Sanchez, S. Wang, Appl. Phys. Lett. 84 (2004) 338.

[12] P. Alpuim, L.M. Gonc¸ alves, E.S. Marins, T.M.R. Viseu, S. Ferdov, J.E. Bourée, Thin Solid Films 517 (2009) 3503.

[13] J.E. Bourée, J. Guillet, C. Grattepain, J. Chaumont, Thin Solid Films 430 (2003) 110.

[14] C.J. Arendse, D. Knoesen, D.T. Britton, Thin Solid Films 501 (2006) 92.

[15] N. Maley, Phys. Rev. B 46 (1992) 2078.

[16] M.H. Brodsky, M. Cardona, J.J. Cuomo, Phys. Rev. B 16 (1977) 3556.

[17] G.G. Stoney, Proc. R. Soc. London A 82 (1909) 172.

[18] K. Takimoto, A. Fukuta, Y. Yamamoto, N. Yoshida, T. Itoh, S. Nonomura, J. Non-Cryst. Solids 299–302 (2002) 314.

[19] T.F.G. Muller, C.J. Arendse, S. Halindintwali, D. Knoesen, R.E.I. Schropp, Thin Solid Films 519 (2011) 4462.

[20] A. Kshirsagar, P. Nyaupane, D. Bodas, S.P. Gangal, Appl. Surf. Sci. 257 (2011) 5052.

[21] E. Zeiler, S. Schwarz, S.M. Rosiwal, R.F. Singer, Mater. Sci. Eng. A-Struct. A335 (2002) 236.

[22] C.H.M. van der Werf, P.A.T.T. van Veenendaal, M.K. van Veen, A.J. Hardeman, M.Y.S. Rusche, J.K. Rath, R.E.I. Schropp, Thin Solid Films 430 (2003) 46.

[23] I. Langmuir, J. Am. Chem. Soc. 34 (1912) 860.

http://repository.uwc.ac.za

[24] A. Gallagher, Thin Solid Films 395 (2001) 25.
[25] E. Bustarret, M. Bensouda, M.C. Habrard, J.C. Bruyère, S. Poulin, S.C. Gujrathi, Phys. Rev. B 38 (1988) 8171.
[26] V. Verlaan, C.H.M. van der Werf, W.M. Arnoldbik, H.D. Goldbach, R.E.I. Schropp, Phys. Rev. B 73 (2006) 195333.
[27] H. Matsumura, A. Masuda, H. Umemoto, Thin Solid Films 501 (2006) 58.
[28] W.A. Lanford, M.J. Rand, J. Appl. Phys. 49 (1978) 2473.
[29] Z. Yin, F.W. Smith, Phys. Rev. B 42 (1990) 3666.
[30] J.J. Mei, H. Chen, W.Z. Shen, H.F. Dekkers, J. Appl. Phys. 100 (2006) 073516.
[31] C.J. Oliphant, C.J. Arendse, D. Knoesen, T.F.G. Muller, S. Prins, G. Malgas, Thin Solid Films 519 (2011) 4437.
[32] R.E.I. Schropp, M. Zeman, Amorphous and Microcrystalline Silicon Solar Cells: Modelling, Materials and Device Technology, Kluwer Academic, Boston, 1998.
[33] A.K. Panchal, C.S. Solanki, J. Cryst. Growth 311 (2009) 2659.
[34] F.W. Smith, Z. Yin, J. Non-Cryst. Solids 137–138 (1991) 871.
[35] Verlaan, Z.S. Houweling, C.H.M. van der Werf, H.D. Goldbach, R.E.I. Schropp, MRS Proc. 910 (2006), 0910-A03-03.
[36] B. Stannowski, J.K. Rath, R.E.I. Schropp, J. Appl. Phys. 93 (2003) 2618.
[37] R.E.I. Schropp, S. Nishizaki, Z.S. Houweling, V. Verlaan, C.H.M. van der Werf, H. Matsumura, Solid State Electron. 52 (2008) 427.
[38] H. Umemoto, T. Morimoto, M. Yamawaki, Y. Masuda, A. Masuda, H. Matsumura, Thin Solid Films 430 (2003) 24.
[39] M.S. Valipa, T. Bakos, E.S. Aydil, D. Maroudas, Phys. Rev. Lett. 95 (2005) 216102.
[40] L.V. Mercaldo, E.M. Esposito, P.D. Veneri, G. Fameli, S. Mirabella, G. Nicotra, Appl. Phys. Lett. 97 (2010) 153112.
[41] J. Bandet, B. Despax, M. Caumont, J. Appl. Phys. 85 (1999) 7899.
[42] M. Luysberg, P. Hapke, R. Carius, F. Finger, Philos. Mag. A 75 (1997) 31. [43] P. Mishra, K.P. Jain, Phys. Rev. B 64 (2001) 073304.
[44] R.P. Wang, G. Xu, P. Jin, Phys. Rev. B 63 (2004) 113303.
[45] H.N. Wanka, M.B. Schubert, MRS Proc. 467 (1997) 651.
[46] H. Fukuda, M. Yasuda, T. Iwabuchi, S. Ohno, Appl. Surf. Sci. 60/61 (1992) 359.
[47] S. Hasegawa, Y. Amano, T. Inokuma, Y. Kurata, J. Appl. Phys. 72 (1992) 5676.
[48] A. Fontcuberta i Morral, P. Roca i Cabarrocas, Thin Solid Films 383 (2001) 161.
[49] B. Swatowska, T. Stapinski, Vacuum 82 (2008) 942.
[50] I.V. Afanasyev-Charkin, M. Nastasi, Nucl. Instrum. Methods B 206 (2003) 736.

http://repository.uwc.ac.za